

# 1 Supplementary material

## 2 Biogeomorphic modeling to assess 3 resilience of tidal marsh restoration to sea 4 level rise and sediment supply

5 Olivier Gourgue<sup>1,2</sup>, Jim van Belzen<sup>3,1</sup>, Christian Schwarz<sup>4</sup>, Wouter Vandenbruwaene<sup>5</sup>, Joris  
6 Vanlede<sup>5</sup>, Jean-Philippe Belliard<sup>1</sup>, Sergio Fagherazzi<sup>2</sup>, Tjeerd J. Bouma<sup>3</sup>, Johan van de  
7 Koppel<sup>3,6</sup>, Stijn Temmerman<sup>1</sup>

8 <sup>1</sup> *Ecosystem Management Research Group, University of Antwerp, Antwerp, Belgium*

9 <sup>2</sup> *Department of Earth and Environment, Boston University, Boston, MA, United States of America*

10 <sup>3</sup> *Department of Estuarine and Delta Systems, NIOZ Royal Netherlands Institute for Sea Research, Yerseke, The  
11 Netherlands*

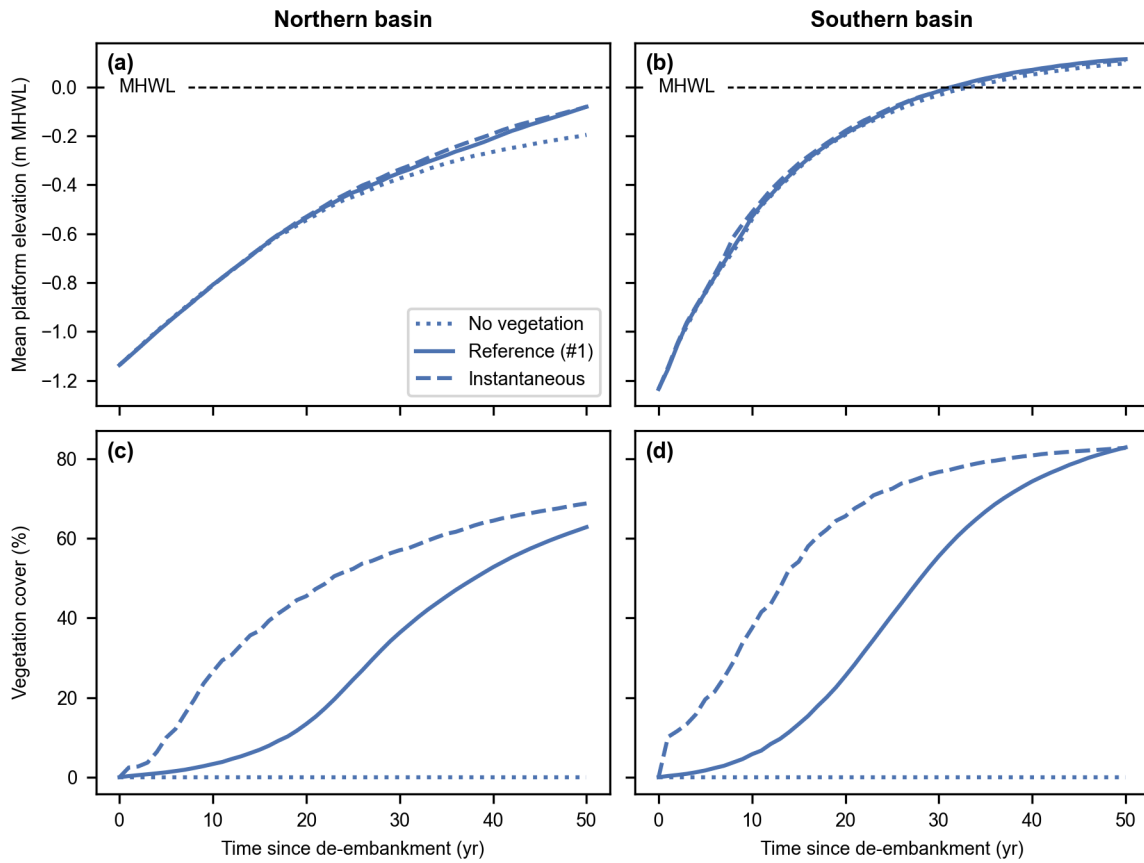
12 <sup>4</sup> *College of Earth, Ocean and Environment, University of Delaware, Lexas, DE, United States of America*

13 <sup>5</sup> *Flanders Hydraulics Research, Antwerp, Belgium*

14 <sup>6</sup> *Conservation Ecology Group, Groningen Institute for Evolutionary Life Sciences, University of Groningen,  
15 Groningen, The Netherlands*

## 16 Content

- 17 • Figures S1 to S7
- 18 • Table S1
- 19 • Sections S1 to S4



20

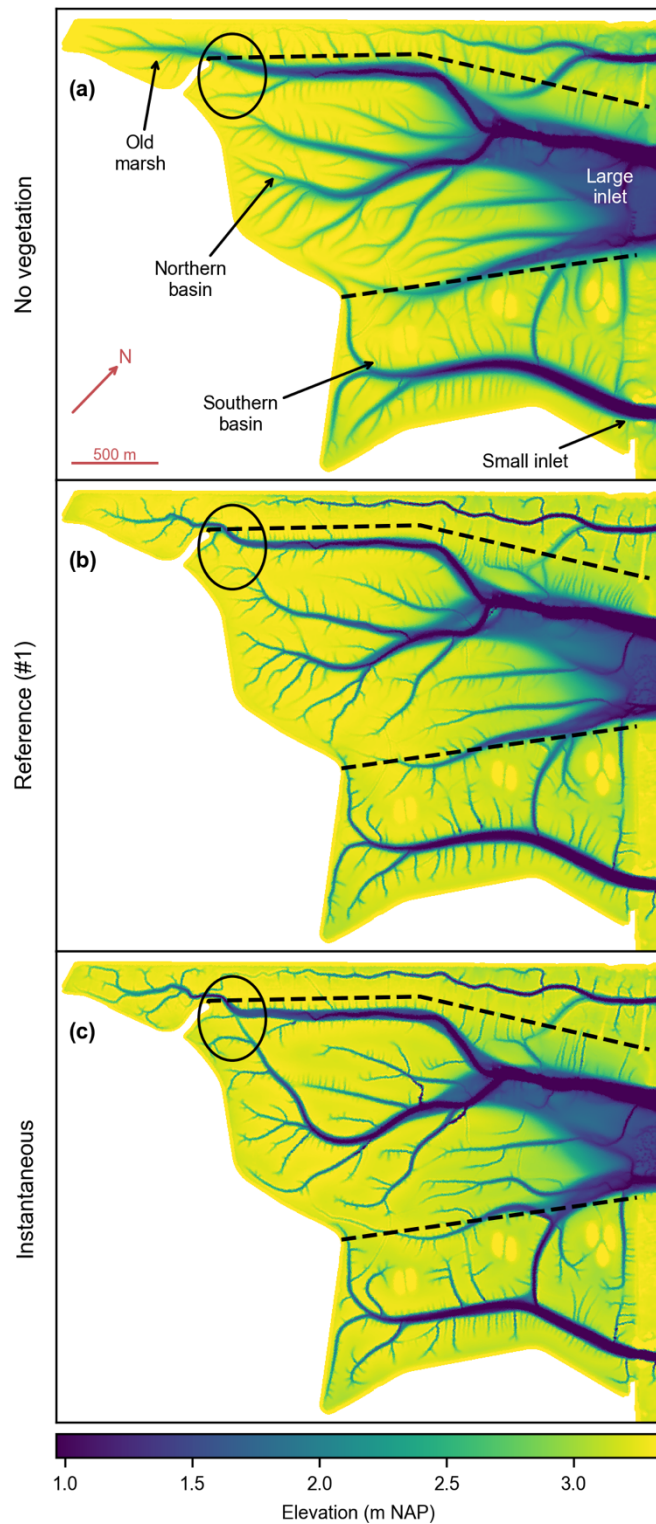
21

22

23

24

Figure S1: Vegetation dynamics model scenarios (i.e., reference vegetation dynamics and two variants, respectively without vegetation and with instantaneous colonization – Sect. 2.3.3). Evolution of the mean platform elevation with respect to the mean high-water level (MHWL) (a-b) and development of the vegetation cover (c-d) in the Northern (a, c) and Southern basins (b, d).



25

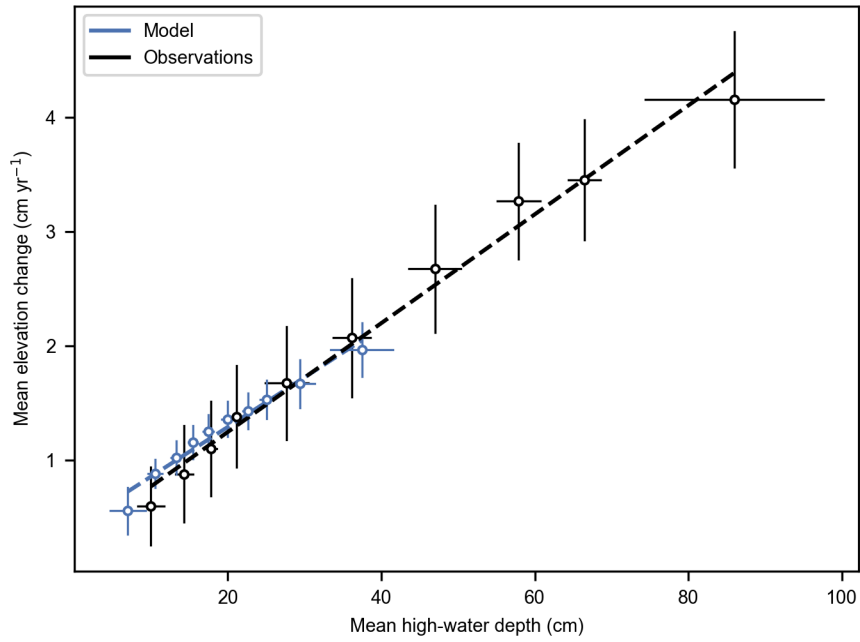
26 Figure S2: Vegetation dynamics model scenarios (i.e., reference vegetation dynamics (a) and two variants, respectively

27 without vegetation (b) and with instantaneous colonization (c) – Sect. 2.3.3). Bed elevation 50 years after de-embankment.

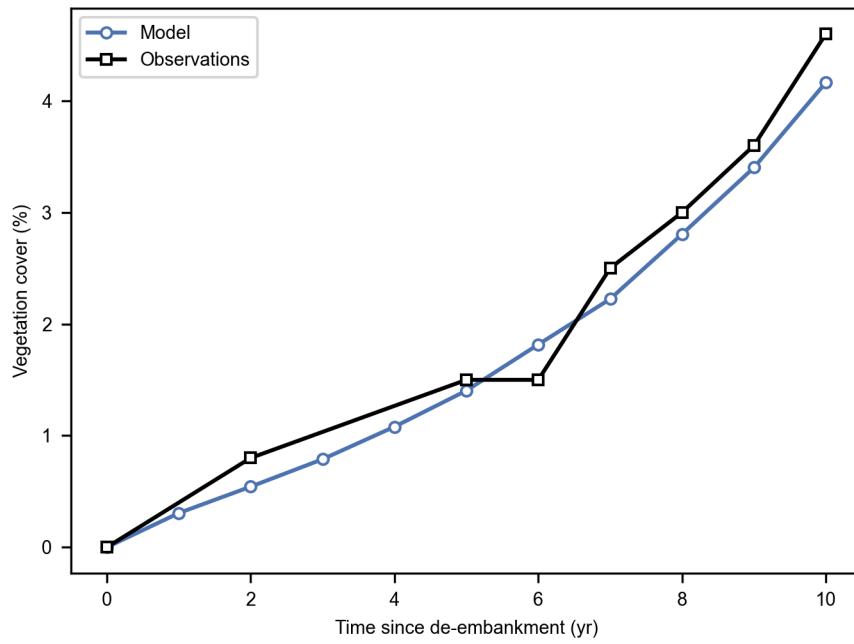
28 The dashed lines delineate the old marsh, the Northern basin, and the Southern basin. The ellipses emphasize a pre-

29 excavated channel that has disappeared (a-b) or survived (c), depending on the vegetation dynamics. All figures are rotated

30 by 43° clockwise, as compared to Fig. 2c.



31  
 32 Figure S3: Reference model scenario (#1). Mean elevation change (between years 18 and 50 for model results, between 1931  
 33 and 1963 for observations) vs. mean high-water depth (in year 18 for model results, in 1931 for observations). Model results  
 34 and observations are respectively split into 10 sub-samples of equal size (Sect. 2.4.4). Markers and error bars represent the  
 35 means and standard deviations of each sub-sample. Dashed lines represent linear regressions of the sub-sample means.  
 36 Model results are on grid nodes that remained vegetated between years 18 and 50. Observations are from areas that remain  
 37 vegetated between years 1931 and 1963 in an established marsh nearby the study site (Sect. 2.4.1) and have been rescaled  
 38 to account for differences in SSC in both sites (Sect. S2).

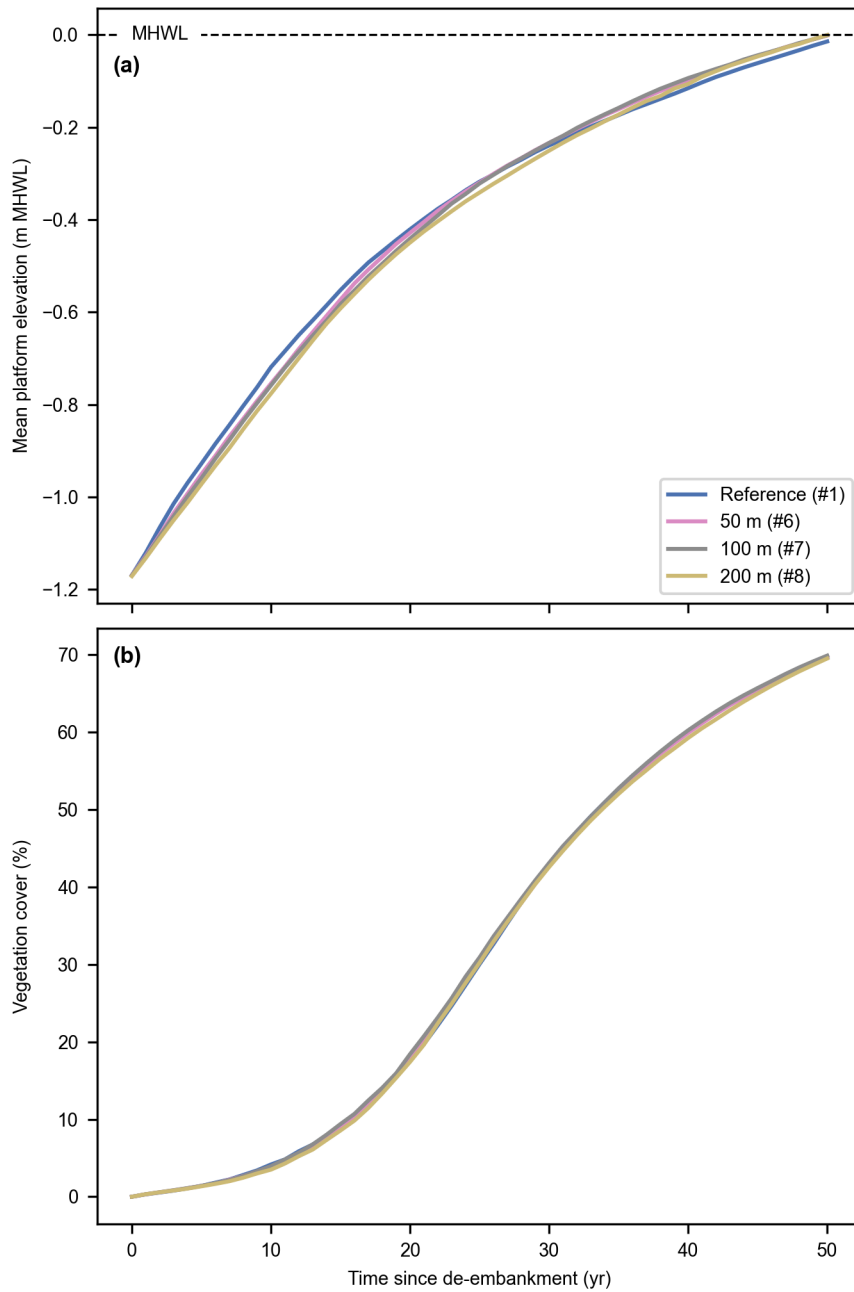


39

40

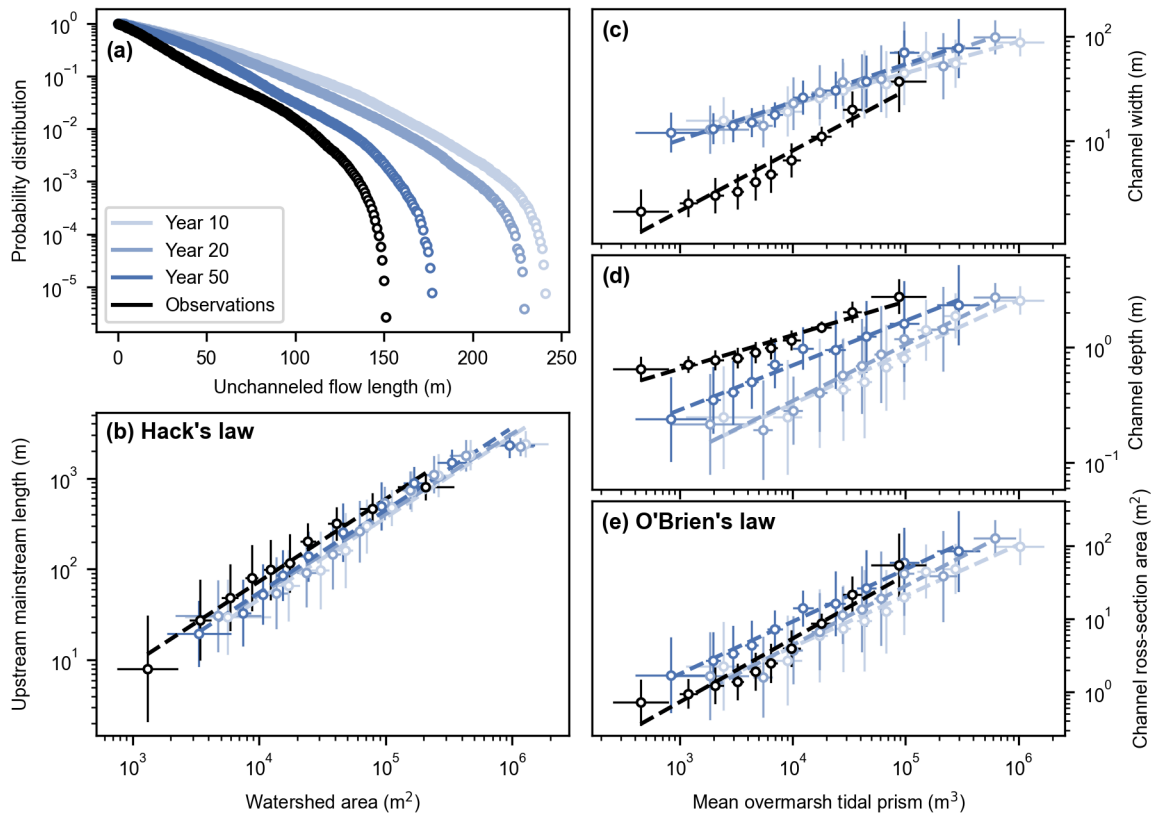
41

Figure S4: Reference model scenario (#1). Development of vegetation cover after de-embankment (blue) compared to observations in another restored marsh close to the study site (black).



42  
 43  
 44  
 45  
 46

Figure S5: Inlet design model scenarios (i.e., reference design and three alternative designs with small-inlet breach size of respectively 50, 100 and 200 m, and excavated channel – #1, 6-8). Evolution of the mean platform elevation with respect to the mean high-water level (MHWL) (a) and development of the vegetation cover (b) in the Northern and Southern basins combined.



47

48

49

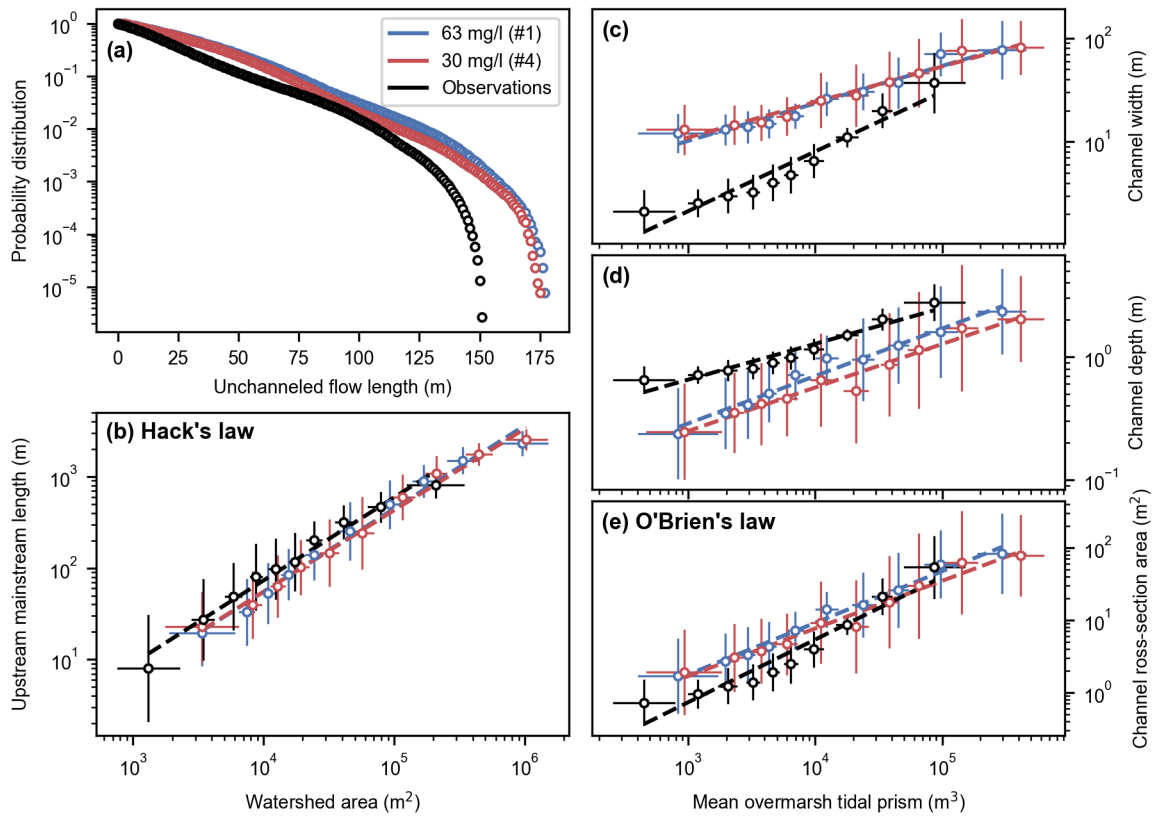
50

51

52

53

Figure S6: Reference model scenario (#1). Channel geometric properties 10, 20 and 50 years after de-embankment (different shades of blue) compared to observations in an established marsh nearby the study site (black). Probability distribution of the unchanneled flow length (a), upstream mainstream length vs. watershed area (b), and channel width (c), channel depth (d) and channel cross-section area (e) vs. mean overmarsh tidal prism. (b-e) Model results and observations are respectively split into 10 sub-samples of equal size (Sect. 2.4.4). Markers and error bars represent the geometric means and standard deviations of each sub-sample. Dashed lines represent geometric regressions of the geometric means.



54  
 55 Figure S7: Suspended sediment concentration model scenarios (#1, 4). Channel geometric properties 50 years after de-  
 56 embankment (blue, red) compared to observations in an established marsh nearby the study site (black). Probability  
 57 distribution of the unchanneled flow length (a), upstream mainstream length vs. watershed area (b), and channel width (c),  
 58 channel depth (d) and channel cross-section area (e) vs. mean overmarsh tidal prism. (b-e) Model results and observations  
 59 are respectively split into 10 sub-samples of equal size (Sect. 2.4.4). Markers and error bars represent the geometric means  
 60 and standard deviations of each sub-sample. Dashed lines represent geometric regressions of the geometric means.

61 Table S1: Coefficients of determination ( $R^2$ ) of the linear regressions obtained from model results and observations in Fig. 4  
 62 and S3, and  $p$ -values of the ANCOVA performed to determine whether linear regressions from model results and  
 63 observations are statistically equal (both  $p$ -values must be higher than 0.05). The first  $p$ -value determines whether the slopes  
 64 of the linear regressions are significantly different (if  $p < 0.05$ ) and the second  $p$ -value whether their intercepts are  
 65 significantly different (if  $p < 0.05$ ).

Figure	$R^2$ (model)	$R^2$ (observations)	$p$ (slopes)	$p$ (intercepts)
Figure 4b	0.985	0.977	0.913	0.007
Figure 4c	0.955	0.929	0.001	< 0.001
Figure 4d	0.973	0.929	0.056	< 0.001
Figure 4e	0.985	0.929	0.023	0.004
Figure S2	0.966	0.987	0.496	0.412

66

## 67 S1 Biogeomorphic model

68 We have developed the biogeomorphic modeling framework Demeter to simulate explicitly  
69 the feedbacks between hydrodynamics, morphodynamics (Sect. S1.1) and vegetation  
70 dynamics (Sect. S1.2). This is a multiscale approach, in which the vegetation dynamics is  
71 computed at much finer resolution than the hydro-morphodynamics (Fig. 1), requiring the  
72 development of specific multiscale coupling techniques to preserve subgrid-scale  
73 heterogeneity while information is exchanged between the hydro-morphodynamic and  
74 vegetation modules (Sect. S1.3 and S1.4). The specific setup for our study site is detailed in  
75 Sect. S1.5.

### 76 S1.1 Telemac (hydro-morphodynamics)

77 As hydro-morphodynamic module (Fig. 1a), we use the finite element solver suite Telemac  
78 (version 7.3.0), and more specifically its modules Telemac-2D for the hydrodynamics and  
79 Sisyphe for the sediment transport and the morphodynamics.

80 Telemac-2d solves the depth-averaged shallow water equations in a two-dimensional  
81 horizontal framework (Hervouet, 2007) to simulate fluctuations of the water depth  $h$  and the  
82 depth-averaged flow velocity  $\mathbf{u}$ :

$$\frac{\partial h}{\partial t} + \nabla \cdot (h\mathbf{u}) = 0 \quad (\text{S1})$$

$$\frac{\partial \mathbf{u}}{\partial t} + \mathbf{u} \cdot \nabla \mathbf{u} = -g\nabla\eta + \frac{1}{h}\nabla \cdot (h\nu\nabla\mathbf{u}) - \frac{\boldsymbol{\tau}_b + \boldsymbol{\tau}_v}{\rho h} \quad (\text{S2})$$

83 where  $t$  is the time,  $\nabla$  is the spatial differential operator,  $g$  is the gravitational acceleration,  
84  $\eta$  is the water surface elevation above the reference level (NAP),  $\nu$  is the diffusion coefficient,  
85  $\boldsymbol{\tau}_b$  is the bed shear stress,  $\boldsymbol{\tau}_v$  is the vegetation resistance force per unit horizontal area, and  
86  $\rho$  is the water density. The bed shear stress is computed with the Manning formula:

$$\boldsymbol{\tau}_b = \frac{\rho g n^2}{h^{1/3}} \|\mathbf{u}\| \mathbf{u} \quad (\text{S3})$$

87 where the Manning coefficient  $n$  is empirically derived and depends mainly on bed roughness.  
88 The vegetation resistance force is modeled as the drag force on a random or staggered array  
89 of rigid cylinders with uniform properties (Baptist et al., 2007) and depends on the spatial  
90 distribution of vegetation provided by the cellular automaton (Sect. S1.4).

91 Sisyphe solves the depth-averaged advection-diffusion equation to simulate fluctuations  
92 of the depth-averaged suspended sediment concentration  $C$ :

$$\frac{\partial hC}{\partial t} + \nabla \cdot (h\mathbf{u}C) = \nabla \cdot (h\nu\nabla C) + E - D \quad (S4)$$

93 where  $E$  and  $D$  are the rates of sediment erosion and deposition, respectively. The rate of  
 94 sediment erosion is computed using the equation of [Partheniades \(1965\)](#):

$$E = \begin{cases} M \left( \frac{\|\boldsymbol{\tau}_b\|}{\tau_e} - 1 \right) & \text{if } \|\boldsymbol{\tau}_b\| > \tau_e \\ 0 & \text{otherwise} \end{cases} \quad (S5)$$

95 where  $M$  is the Partheniades constant and  $\tau_e$  is the critical bed shear stress for sediment  
 96 erosion. The rate of sediment deposition is computed using the equation of [Einstein and  
 97 Krone \(1962\)](#):

$$D = w_s C \quad (S6)$$

98 where  $w_s$  is the sediment settling velocity. The evolution of the bed is computed as follows:

$$\frac{\partial b}{\partial t} = \alpha \frac{D - E}{\rho_s} \quad (S7)$$

99 where  $b$  is the bed surface elevation above the reference level (NAP),  $\alpha$  is the morphological  
 100 acceleration factor ([Sect. 2.1](#)) and  $\rho_s$  is the sediment dry bulk density. The bed is composed  
 101 of two layers: the fresh layer at the surface and the compacted layer underneath. Their  
 102 evolution obeys the following rules: (i) each layer is characterized by different values of  $\tau_e$   
 103 and  $\rho_s$ , (ii) erosion of the compacted layer only occurs where and when the fresh layer is  
 104 locally empty, (iii) deposition only occurs on the fresh layer, and (iv) there is no sediment flux  
 105 between the two layers.

## 106 [S1.2 Cellular automaton \(vegetation dynamics\)](#)

107 As vegetation module, we use the cellular automaton implemented in Demeter. A cellular  
 108 automaton consists of a regular grid of cells, each one with a finite number of states (here,  
 109 either bare or one of the considered vegetation species). Cells can change their state in  
 110 discrete time steps, depending on their neighborhood state and a set of simple stochastic  
 111 transition rules ([Balzter et al., 1998](#)).

### 112 [S1.2.1 Establishment](#)

113 Establishment is the transition from bare state 0 to any vegetated state  $i$ . The probability of  
 114 establishment  $p_i^{est}$  for species  $i$  is evaluated as:

$$p_i^{est} = P_i^{est} \prod_k f_k \quad (S8)$$

115 where  $P_i^{est}$  is the background probability of establishment for species  $i$ , and  $f_k$  are stress  
 116 functions of the environmental variables (Sect. S1.2.5).

### 117 S1.2.2 Succession

118 Succession is the transition from any vegetated state  $i$  to another vegetated state  $j > i$  (e.g.,  
 119 from pioneer to climax vegetation). The probability of succession  $p_{i,j}^{suc}$  from species  $i$  to  $j$  is  
 120 evaluated as:

$$p_{i,j}^{suc} = P_{i,j}^{suc} \prod_k f_k \quad (S9)$$

121 where  $P_{i,j}^{suc}$  is the background probability of succession from species  $i$  to  $j$ .

### 122 S1.2.3 Stress-related die-off

123 Stress-related die-off (or simply die-off) is the transition from any vegetated state  $i$  to bare  
 124 state 0 due to environmental stress. The probability of die-off  $p_i^{die}$  for species  $i$  is evaluated  
 125 as follows:

$$p_i^{die} = 1 - \prod_k (1 - f_k) \quad (S10)$$

### 126 S1.2.4 Annual die-off

127 Annual die-off is the transition from any vegetated state  $i$  to bare state 0 due to the natural  
 128 cycle of annual species. The probability of annual die-off  $p_i^{ann}$  for species  $i$  is evaluated as  
 129 follows:

$$p_i^{ann} = P_i^{ann} \quad (S11)$$

130 where  $P_i^{ann}$  is the background probability of annual die-off for species  $i$ .

### 131 S1.2.5 Stress functions

132 Stress functions (Sect. S1.2.1 to S1.2.3) can be of two shapes. When vegetation is only  
 133 affected at high (resp. low) values of an environmental stressor, and not below (resp. above)  
 134 a certain threshold, we use the Hill function, which varies from 0 to 1 following:

$$f_H(x; H, N) = \frac{x^N}{H^N + x^N} \quad (S12)$$

135 where  $x$  is the environmental variable,  $H$  is the threshold around which the transition from 0  
 136 to 1 occurs, and  $N$  is a parameter that controls the shape of the function. The function  
 137 decreases from 1 to 0 if  $N < 0$  and increases from 0 to 1 if  $N > 0$ . The transition from 0 to 1  
 138 becomes steeper for increasing  $|N|$ .

139 When the range of optimal conditions is confined between a low and a high threshold  
 140 value, we use the Brière function:

$$f_B(x; X_0, X_1) = \max\left(\frac{x(x - X_0)(X_1 - x)}{c}, 0\right) \quad (S13)$$

141 where  $X_0$  and  $X_1$  are the low and high thresholds, respectively, and  $c$  is a coefficient used to  
 142 rescale the function, so that its maximum value is 1:

$$c = x_{opt}(x_{opt} - X_0)(X_1 - x_{opt}) \quad (S14)$$

$$x_{opt} = \frac{1}{3}\left(X_0 + X_1\sqrt{X_1^2 - X_0X_1 + X_0^2}\right) \quad (S15)$$

143 The different environmental variables used for the stress functions are the hydroperiod,  
 144 the bed elevation gain and loss, and the binned shear stress (Sect. S1.3.1).

#### 145 S1.2.6 Lateral expansion

146 Lateral expansion is the transition from any state  $i$  (bare or vegetated) to any vegetated state  
 147  $j > i$  resulting from the presence of at least one neighboring cell of state  $j$ . The recruitment  
 148 process is here quite different than for the other processes. It is defined by the mean  
 149 expansion rate  $R_i^{exp}$ , which determines the number of iterations  $N_{exp}$  of the cellular  
 150 automaton. For each iteration, the probability of recruitment by lateral expansion  $p_i^{exp}$  is

$$p_i^{exp} = \frac{R_i^{exp}}{N_{exp}\Delta x} \quad (S16)$$

151 where  $\Delta x$  is the grid resolution of the cellular automaton. With this stochastic approach, even  
 152 though the mean expansion rate is constant, the actual expansion rate varies in space and  
 153 time. The number of iterations is determined so that

$$R_{max} > R_i^{exp} + 2\sigma^2 \quad (S17)$$

154 where the maximum expansion rate  $R_{max}$  and the variance of the expansion rate  $\sigma^2$  are  
 155 calculated as follows:

$$R_{max} = N_{exp}\Delta x \quad (S18)$$

$$\sigma^2 = N_{exp}p_i^{exp}(1 - p_i^{exp})\Delta x = R_i^{exp}\left(1 - \frac{R_i^{exp}}{N_{exp}\Delta x}\right) \quad (S19)$$

156 As each species can have a different mean expansion rate, and hence a different number of  
 157 iterations, we use the highest number of iterations among all species.

#### 158 S1.2.7 Computational sequence

159 The different transition rules of the cellular automaton are scheduled as follows:

- 160 1. Annual die-off is applied for each annual species in one single iteration.
- 161 2. Establishment, succession, and lateral expansion are applied for all species in an
- 162 iterative process. The number of iterations is determined based on the mean
- 163 expansion rates (Sect. S1.2.6). For each iteration, the probabilities of establishment,
- 164 succession and lateral expansion are rescaled as follows:

$$p_i^{est} \leftarrow 1 - (1 - p_i^{est})^{N_{exp}} \quad (S20)$$

$$p_{i,j}^{suc} \leftarrow 1 - (1 - p_{i,j}^{suc})^{N_{exp}} \quad (S21)$$

$$p_i^{exp} \leftarrow p_i^{exp} \frac{N_{nb}}{4} \quad (S22)$$

165 where  $N_{nb}$  is the number of neighboring cells vegetated with the same species  $i$  at

166 the previous iteration. We use a factor  $\frac{1}{4}$  in Eq. S22, so that the rescaling factor  $\frac{N_{nb}}{4}$  is

167 1 on average.

- 168 3. Stress-related die-off is then applied in one single iteration.

### 169 S1.3 Coupling Telemac to cellular automaton

#### 170 S1.3.1 Environmental variables

171 The hydroperiod  $T_H$  is the percentage of time during which a Telemac grid node is flooded

172 (i.e., the water depth higher than 0.1 m) between two cellular automaton calls. It varies

173 between 0 (never flooded) and 1 (always flooded).

174 The bed elevation change  $\Delta b$  is the difference between the final and initial bed elevations

175 between two cellular automaton calls. The bed elevation gain  $\Delta b_+$  and the bed elevation loss

176  $\Delta b_-$  are calculated as:

$$\Delta b_+ = \max(\Delta b, 0) \quad (S23)$$

$$\Delta b_- = \max(-\Delta b, 0) \quad (S24)$$

177 The binned shear stress is calculated by classifying flow directions into 8 directional bins

178 ( $45^\circ$  each) occurring between two cellular automaton calls. The relative binned time  $T^i$ , the

179 binned shear stress  $\bar{\tau}_b^i$ , and the binned water depth  $\bar{h}^i$  are respectively the percentage of

180 time, the mean bed shear stress, and the mean water depth when the flow is oriented in the

181  $i^{\text{th}}$  bin. As bed shear stress and flow directions are especially relevant above certain thresholds

182 of the water depth and the bed shear stress, these binned variables only account for

183 situations when the water depth is higher than 0.1 m and the bed shear stress is higher than

184  $0.1 \text{ N m}^{-2}$ .

185 The mean water depth  $\bar{h}$  between two cellular automaton calls is calculated for situations  
 186 when the water depth is higher than 0.1 m.

### 187 S1.3.2 Spatial refinement

188 We use a linear interpolation to spatially refine the hydroperiod, and the bed elevation gain  
 189 and loss from the Telemac grid to the cellular automaton grid.

190 We use the concepts of Voronoi neighborhood to spatially refine the relative binned time  
 191 and the binned water depth. Each cellular automaton grid cell is associated with its closest  
 192 Telemac grid node. The Voronoi neighborhood of a Telemac grid node is the ensemble of all  
 193 associated cellular automaton grid cells. Here, the relative binned time and the binned water  
 194 depth of a Telemac grid node are passed to all cellular automaton grid cells of its Voronoi  
 195 neighborhood.

196 For the binned shear stress, we use a convolution method that allows to account for  
 197 interactions between flow and subgrid-scale vegetation patterns (Gourgue et al., 2021).  
 198 Practically, we first calculate the binned velocity  $\bar{u}^i$  on the Telemac grid as follows:

$$\bar{u}^i = \left( \frac{\bar{\tau}_b^i (\bar{h}^i)^{1/3}}{\rho g n^2} \right)^{1/2} \quad (S25)$$

199 Then, we use a convolution method (Gourgue et al., 2021) to spatially refine the mean binned  
 200 velocity from the Telemac grid to the cellular automaton grid. Finally, we calculate the binned  
 201 shear stress on the Telemac grid as follows:

$$\bar{\tau}_b^i = \frac{\rho g n^2}{(\bar{h}^i)^{1/3}} (\bar{u}^i)^2 \quad (S26)$$

### 202 S1.3.3 Stress function of the binned shear stress

203 A stress function of the binned shear stress (typically using the Hill function) requires a specific  
 204 treatment to combine all its components. It is calculated as follows:

$$f = 1 - \prod_{i=1}^8 \left( 1 - f_H(\bar{\tau}_b^i; H, N) \right)^{T^i} \quad (S27)$$

## 205 S1.4 Coupling cellular automaton to Telemac

### 206 S1.4.1 Vegetation resistance force

207 For the vegetation resistance force per unit horizontal area  $\tau_v$  in Eq. S2 of the hydro-  
 208 morphodynamic module, we use the approach introduced by Baptist et al. (2007), which

209 considers plants as rigid cylinders with uniform morphological properties (i.e., stem density,  
 210 diameter and height). As compared to the original method, we here neglect the extra term  
 211 depending on the ratio between water depth and plant height, and we combine linearly the  
 212 separate effect of each plant species:

$$\tau_v = \frac{1}{2} \rho \beta \left( \sum_i C_{Di} \gamma_i m_i d_i \min(h, k_i) \right) \| \mathbf{u} \| \mathbf{u} \quad (\text{S28})$$

213 where  $\beta$  is the transmittance coefficient (Sec. S1.4.2), and  $C_{Di}$ ,  $\gamma_i$ ,  $m_i$ ,  $d_i$  and  $k_i$  are  
 214 respectively the bulk drag coefficient (Baptist et al., 2007), the vegetation cover (Sec. S1.4.2),  
 215 the stem density, the stem diameter and the stem height of species  $i$ .

#### 216 S1.4.2 Spatial coarsening

217 The vegetation cover  $\gamma_i$  of the species  $i$  is the percentage of cellular automaton cells of state  
 218  $i$  within the Voronoi neighborhood of a Telemac grid node (Sec. S1.3.2). It varies between 0  
 219 (not covered by species  $i$ ) and 1 (fully covered by species  $i$ ). The sum of all vegetation covers  
 220 also varies between 0 (bare) and 1 (fully covered by vegetation).

221 The transmittance coefficient  $\beta$  accounts for the spatial heterogeneity of the vegetation  
 222 distribution at the subgrid scale (i.e., within a Voronoi neighborhood). In general,  
 223 hydrodynamic models assume a uniform spatial distribution at the subgrid scale (here,  $\beta =$   
 224 1), which leads to considerable overestimation of the flow resistance if the vegetation  
 225 presents clustered patterns at the subgrid scale (Gourgue et al, 2019). The method to  
 226 compute the transmittance coefficient  $\beta$  builds on the similarity between the Chézy formula  
 227 in fluid dynamics and Ohm's law in electricity. Taking the analogy further, we recalculate the  
 228 coarse-scale hydraulic roughness just as the total resistance of an electronic circuit that  
 229 combines resistors (equivalent to cellular automaton cells in our analogy) connected in series  
 230 (along-flow) and in parallel (across-flow). The transmittance coefficient  $\beta$  is calculated at the  
 231 end of a cellular automaton call. It varies between 0 and 1 and it has different values  
 232 depending on the flow direction (Gourgue et al, 2019).

### 233 S1.5 Study site setup

#### 234 S1.5.1 Hydro-morphodynamic module

235 The initial bed elevation is based on the project design (Sec. 2.2 and Fig. 2) and Lidar data  
 236 before de-embankment. The bed is initially exclusively composed of a compacted layer. Tides

237 are imposed into the system by defining water levels and flow velocities at the open boundary  
238 between the study site and the Scheldt Estuary, which is here approximately the isobath 5 m  
239 below the mean low water level. These boundary conditions are provided by a 3D  
240 hydrodynamic model of the estuary, which has been calibrated for a spring-neap cycle by  
241 comparison with measurements of water levels, flow velocities and water discharges  
242 ([Maximova et al., 2014](#)). To reduce the computational time, we do not simulate the entire  
243 range of tidal conditions of a full spring-neap cycle. Instead, we only select four different semi-  
244 diurnal tidal cycles from the estuarine model, which are representative of the standard range  
245 of tidal conditions that can be observed in that area. With high water levels of 2.05, 2.55, 2.87  
246 and 3.25 m NAP, the selected tidal cycles have a frequency distribution of respectively 14.6%,  
247 27.4%, 32.3% and 25.7%, as compared to historical measurements during the period 2007-  
248 2017. These frequency distributions are then used to determine the morphological  
249 acceleration factor  $\alpha$  used for each semi-diurnal tidal cycle ([Sec. 2.1](#)). We simulate the impact  
250 of sea level rise by lowering the bed elevation every year by a value corresponding to the  
251 yearly increase of mean sea level. The suspended sediment concentration at the open  
252 boundary is constant and determined based on reported measurements ([Vandenbruwaene  
253 et al., 2014](#); [Sec. S2](#)). All parameter values used in the hydro-morphodynamic module are  
254 summarized in [Table S2](#). The suspended sediment concentration at the open boundary and  
255 the rate of sea level rise vary according to model scenarios ([Table 1](#)).

256 Table S2: Hydro-morphodynamic module parameter values.

Parameter	Symbol	Value	Reference
Gravitational acceleration	$g$	9.81 m s <sup>-2</sup>	Standard
Diffusion coefficient	$\nu$	1 m <sup>2</sup> s <sup>-1</sup>	Calibration
Water density	$\rho$	1000 kg m <sup>-3</sup>	Standard
Manning coefficient	$n$	0.021 s m <sup>-1/3</sup>	Maximova et al., 2014
Partheniades constant	$M$	10 <sup>-4</sup> kg m <sup>2</sup> s <sup>-1</sup>	D'Alpaos et al., 2012; Zhou et al., 2016
Critical bed erosion shear stress	$\tau_e$	0.5 N m <sup>-2</sup> (fresh layer)	Zhou et al., 2016
		0.8 N m <sup>-2</sup> (compacted layer)	Zhou et al., 2016; D'Alpaos et al., 2012
Settling velocity	$w_s$	1 mm s <sup>-1</sup>	van Leussen, 1999
Morphological acceleration factor	$\alpha$	103 (neap tide)	Sec. 2.1 and S1.5
		193.5 (mid-neap tide)	
		228 (mid-spring tide)	
		181.5 (spring tide)	
Dry bulk density	$\rho_s$	500 kg m <sup>-3</sup> (fresh layer)	Van de Broek et al., 2018
		1500 kg m <sup>-3</sup> (compacted layer)	
Bulk drag coefficient	$C_D$	2 (pioneer marsh)	Calibration (Gourgue et al., 2021) with flume measurements (Schwarz et al., 2015)
		1 (middle marsh)	
		5 (high marsh)	
Stem density	$m$	214 m <sup>-2</sup> (pioneer marsh)	Field observations
		338 m <sup>-2</sup> (middle marsh)	
		298 m <sup>-2</sup> (high marsh)	
Stem diameter	$d$	12 mm (pioneer marsh)	Field observations
		6.8 mm (middle marsh)	
		5.98 mm (high marsh)	
Stem height	$k$	1 m (pioneer marsh)	Field observations
		1.03 m (middle marsh)	
		2.36 m (high marsh)	

257

## 258 S1.5.2 Vegetation module

259 The study site is in the oligohaline zone (0.5 – 5 PSU) where *Aster tripolium* is often  
260 observed as the pioneer species, and *Scirpus maritimus* and *Phragmites australis* in the marsh  
261 interior (Van Braeckel et al., 2008). Their expected encroachment in our study site is further  
262 supported by the results of transplantation experiments carried out in nearby tidal marshes.  
263 *Aster tripolium* is an annual species, which can be found as lower pioneer in calm areas and  
264 along creek edges. It colonizes the tidal flats and creek levees every year from seeds, as  
265 randomly scattered high density clusters on tidal flats. Although it is regarded as an annual  
266 species, part of the established plants can survive and develop for another year. *Scirpus*  
267 *maritimus* is the dominant perennial species from the low pioneer zone into the middle marsh  
268 zone. It is even the only species present in the pioneer zone in several tidal marshes close to  
269 the study site. The main mode of colonization on bare tidal flats is via lateral spread of  
270 rhizomes (Silinski et al., 2016). *Phragmites australis* is the dominant species in the high marsh  
271 zone. It can form large stands from the high pioneer zone up to the supratidal zone, but it is  
272 mostly found above *Scirpus maritimus* in the middle and high marsh zone. Most seedling  
273 establishment occurs within already established vegetation, but very rarely on bare tidal flats,  
274 except for the highest areas. Once established, it can often outcompete *Scirpus maritimus*  
275 and colonize vegetated areas by lateral expansion via rhizomes, resulting in clearly visible  
276 circular patches within *Scirpus maritimus* marshes.

277 The initial vegetation distribution is based on aerial pictures before de-embankment.  
278 Marshes that will be excavated and farmland are considered as unvegetated.  
279 Parameterization of the different stress functions (Sec. S1.2.5) is based on field and flume  
280 experiments, remote sensing, literature data and model calibration (Tables S3-S4).

Table S3: Vegetation module parameterizations (reference vegetation dynamics, used in model scenarios #1-8).

Process	Contribution	Reference
<i>Aster tripolium</i> (species 1, pioneer marsh)		
Establishment (Eq. S8)	$P_1^{est} = 0.2$	Calibration
	$f_B(T_H; 0.039, 0.1134)$	Field experiments; <a href="#">Silinski et al., 2016</a>
	$f_H(\Delta b_+; 0.03 \text{ m}, -2.37)$ $f_H(\Delta b_-; 0.001 \text{ m}, -4)$	<a href="#">Bouma et al., 2016</a> ; <a href="#">Cao et al. 2018</a>
Die-off (Eq. S10 and S27)	$f_H(T_H; 0.129, 25)$	Field experiments; <a href="#">Silinski et al., 2016</a>
	$f_H(T_H; 0.019, -31)$	
	$f_H(\Delta b_-; 0.02 \text{ m}, 6.32)$ $f_H(\bar{\tau}_b^i; 0.2 \text{ N m}^{-2}, 15)$	<a href="#">Bouma et al., 2016</a> ; <a href="#">Cao et al. 2018</a> Flume experiments; calibration
Annual die-off (Eq. S11)	$P_1^{ann} = 0.5$	Calibration
<i>Scirpus maritimus</i> (species 2, middle marsh)		
Establishment (Eq. S8)	$P_2^{est} = 10^{-5}$	Calibration
	$f_B(T_H; 0.011, 0.105)$	Field experiments; <a href="#">Silinski et al., 2016</a>
	$f_H(\Delta b_+; 0.03 \text{ m}, -2.37)$ $f_H(\Delta b_-; 0.001 \text{ m}, -4)$	<a href="#">Bouma et al., 2016</a> ; <a href="#">Cao et al. 2018</a>
Die-off (Eq. S10 and S27)	$f_H(T_H; 0.38, 40)$	Field experiments; <a href="#">Silinski et al., 2016</a>
	$f_H(T_H; 0.001, -41)$	
	$f_H(\Delta b_-; 0.075 \text{ m}, 4)$ $f_H(\bar{\tau}_b^i; 0.15 \text{ N m}^{-2}, 15)$	<a href="#">Bouma et al., 2016</a> ; <a href="#">Cao et al. 2018</a> Flume experiments; calibration
Lateral expansion	$R_2^{exp} = 2.25 \text{ m}$	Remote sensing; <a href="#">Silinski et al., 2016</a>
<i>Phragmites australis</i> (species 3, high marsh)		
Establishment (Eq. S8)	$P_3^{est} = 5 \times 10^{-7}$	Calibration
	$f_H(T_H; 0.035, -8.5)$	Field experiments; <a href="#">Silinski et al., 2016</a>
	$f_H(\Delta b_+; 0.03 \text{ m}, -2.37)$ $f_H(\Delta b_-; 0.001 \text{ m}, -4)$	<a href="#">Bouma et al., 2016</a> ; <a href="#">Cao et al. 2018</a>
Succession (Eq. S9) (from <i>Scirpus maritimus</i> )	$P_{2,3}^{suc} = 2.5 \times 10^{-6}$	Calibration
	$f_H(T_H; 0.054, -6.5)$	Field experiments; <a href="#">Silinski et al., 2016</a>
	$f_H(\Delta b_+; 0.03 \text{ m}, -2.37)$ $f_H(\Delta b_-; 0.001 \text{ m}, -4)$	<a href="#">Bouma et al., 2016</a> ; <a href="#">Cao et al. 2018</a>
Die-off (Eq. S10 and S27)	$f_H(T_H; 0.13, 20)$	Field experiments; <a href="#">Silinski et al., 2016</a>
	$f_H(\Delta b_-; 0.1 \text{ m}, 6.32)$	<a href="#">Bouma et al., 2016</a> ; <a href="#">Cao et al. 2018</a>
	$f_H(\bar{\tau}_b^i; 0.12 \text{ N m}^{-2}, 15)$	Flume experiments; calibration
Lateral expansion	$R_3^{exp} = 2.25 \text{ m}$	Remote sensing; <a href="#">Silinski et al., 2016</a>

282 Table S4: Vegetation module parameterizations (instantaneous colonization, used in reference model scenario variant).

Process	Contribution	Reference
<i>Aster tripolium</i> (species 1, pioneer marsh)		
Establishment (Eq. S8)	$p_1^{est} = \begin{cases} 1 & \text{if } H < 0.1134 \\ 0 & \text{if } H \geq 0.1134 \end{cases}$	Field experiments; <a href="#">Silinski et al., 2016</a>
Die-off (Eq. S10)	$p_1^{die} = \begin{cases} 0 & \text{if } H < 0.129 \\ 1 & \text{if } H \geq 0.129 \end{cases}$	
<i>Scirpus maritimus</i> (species 2, middle marsh)		
Succession (Eq. S9) (from <i>Aster tripolium</i> )	$p_{1,2}^{suc} = \begin{cases} 1 & \text{if } H < 0.078 \\ 0 & \text{if } H \geq 0.078 \end{cases}$	Field experiments; <a href="#">Silinski et al., 2016</a>
Die-off (Eq. S10)	$p_2^{die} = \begin{cases} 0 & \text{if } H < 0.38 \\ 1 & \text{if } H \geq 0.38 \end{cases}$	
<i>Phragmites australis</i> (species 3, high marsh)		
Succession (Eq. S9) (from <i>Scirpus maritimus</i> )	$p_{2,3}^{suc} = \begin{cases} 1 & \text{if } H < 0.044 \\ 0 & \text{if } H \geq 0.044 \end{cases}$	Field experiments; <a href="#">Silinski et al., 2016</a>
Die-off (Eq. S10)	$p_3^{die} = \begin{cases} 0 & \text{if } H < 0.13 \\ 1 & \text{if } H \geq 0.13 \end{cases}$	

## 283 S2 Sediment accretion on vegetated platforms

284 Based on digital elevation maps derived from historical topographic surveys in the adjacent  
 285 marshes of the Drowned Land of Saefthinghe ([Fig. 2c](#)) between 1931 and 1963 ([Wang and](#)  
 286 [Temmerman, 2013](#)), we have developed an empirical relationship between mean elevation  
 287 change on vegetated platforms and mean high-water depth ([Vandenbruwaene et al., 2014](#)).  
 288 Here, we develop a similar relationship based on model results in the restored tidal marsh,  
 289 using the same variables over the same time interval (i.e., between years 18 and 50 after de-  
 290 embankment), and we compare it with the empirical relationship derived from observations.

291 The digital elevation maps derived from historical topographic surveys have a resolution  
 292 of 20 m. To focus on vegetated platforms and avoid the influence of tidal channels, we only  
 293 consider vegetated areas that are at least 200 m from tidal channels in the digital maps  
 294 ([Vandenbruwaene et al., 2014](#)). Similarly, as our model results have a resolution of 5 m, we  
 295 only consider areas that are at least 50 m from tidal channels in the model results.

296 The Drowned of Saeftinghe is located downstream of the study site, where the sediment  
297 input from the Scheldt Estuary is substantially lower. Historical measurements in the period  
298 2001-2012 reveal that the tide-averaged SSC in the estuary is 42 mg l<sup>-1</sup> close to the Drowned  
299 of Saeftinghe and 63 mg l<sup>-1</sup> close the study site (Vandenbruwaene et al., 2014). To account for  
300 this 1.5 ratio in sediment input between model and observations, we multiply the observed  
301 mean elevation change by 1.5 to obtain the data presented in Fig. S1.

### 302 S3 Pioneer vegetation development

303 We compare our model results with observed rate of spatial expansion of the vegetation  
304 cover in the adjacent restored marshes of Paardenschor (Fig. 2c), from the onset of vegetation  
305 in 2007 until 2017. We use a series of Google Earth images, and we apply the method of  
306 Richardson et al. (2009) to classify vegetation pixels. Part of the vegetation colonization in  
307 Paardenschor starts from the dikes. Such phenomenon is expected to be of a much lesser  
308 influence in our study site. Hedwige-Prosper Polder is about 30 times larger than  
309 Paardenschor, hence the average distance to dikes will be much higher. In our analysis, we  
310 therefore remove the vegetation development occurring from the dikes.

### 311 S4 Channel network characteristics

312 We compare various geometric properties of the simulated tidal channels with observations  
313 in the adjacent marshes of the Drowned Land of Saeftinghe (Fig. 2c – Vandenbruwaene et al.,  
314 2013, 2015). To that end, we have developed a quasi-automatic methodology to extract tidal  
315 channel networks and related characteristics from model results. We first identify grid nodes  
316 within channels by applying a multi-window median neighborhood analysis (Liu et al., 2015)  
317 on the simulated topography, and we compute the unchanneled flow length as the shortest  
318 distance to a channel grid node (Tucker et al., 2001). We then retrieve channel edges as  
319 multiple polygons by applying the Python function tricontour from the visualization library  
320 Matplotlib (Hunter, 2007) on the channel grid nodes. We finally extract the channel network  
321 skeleton, defined as the channel centerlines (Fagherazzi et al., 1999), by generating the raw  
322 Voronoi diagram of the channel edge polygons (with the Python library Centerline) and  
323 applying straightforward threshold rules to simplify it.

324 We use a virtual topography method to determine the watershed areas along the network  
325 skeleton ([Vandenbruwaene et al., 2013, 2015](#)). In terrestrial river networks, watershed areas  
326 are exclusively delineated by topographic gradients. For tidal channel networks, however,  
327 topographic gradients are small and water flow is mainly determined by water surface  
328 gradients ([Rinaldo et al., 1999](#)). Alternatively, algorithms designed for terrestrial river  
329 networks (here the Python library `pysheds`) can be applied on a virtual topography built as  
330 the sum of the shortest distance to the network skeleton and the distance to the mouth along  
331 the network skeleton. For every point along the network skeleton, we can then compute the  
332 watershed area and the upstream mainstream length, defined as the longest upstream  
333 channel within the corresponding watershed.

334 Cross-sectional dimensions of tidal channels are traditionally related to the spring tidal  
335 prism ([D'Alpaos et al., 2010](#)). For tidal marsh channels, however, overmarsh tides that  
336 overtop the intertidal platform are more relevant ([Vandenbruwaene et al., 2013, 2015](#))  
337 because maximum channel flow velocities typically occur when the surrounding platform is  
338 flooded and drained ([French and Stoddart, 1992](#)). Here we use the mean overmarsh tidal  
339 prism, defined as the mean tidal prism from all overmarsh tides. For every point along the  
340 network skeleton, we compute the mean platform elevation of the corresponding watershed.  
341 The mean overmarsh tidal prism is then simply the product between the watershed area and  
342 the mean overmarsh high-water depth, obtained from all simulated high tides higher than  
343 the mean platform elevation.

344 We generate channel cross-sections along the network skeleton by balancing two  
345 constraints: cross-sections must be as perpendicular as possible to the network skeleton and  
346 consecutive cross-sections must not intersect each other. Where both constraints can be met,  
347 we then compute the channel depth as the difference between the mean channel edge  
348 elevation and the lowest cross-section elevation, the channel width as the distance between  
349 channel edges, and the cross-section area as the integral of the difference between the mean  
350 channel edge elevation and the cross-section elevation.

351 Additional references

- 352 D’Alpaos, A., Lio, C.D., and Marani, M.: Biogeomorphology of tidal landforms: Physical and  
353 biological processes shaping the tidal landscape, *Ecohydrology*, 5, 550-562,  
354 <https://doi.org/10.1002/eco.279>, 2012.
- 355 French, J.R. and Stoddart, D.R.: Hydrodynamics of salt marsh creek systems: Implications for  
356 marsh morphological development and material exchange, *Earth Surf. Proc. Land.*, 17,  
357 235-252, <https://doi.org/10.1002/esp.3290170304>, 1992.
- 358 Gourgue, O., van Belzen, J., Schwarz, C., Bouma, T.J., van de Koppel, J., and Temmerman, S.:  
359 A new bio-geomorphic model approach accounting for subgrid-scale heterogeneity of  
360 biogenic structures, *Geophysical Research Abstracts*, 21, EGU2019-16933, 2019.
- 361 Hunter, J.D.: Matplotlib: A 2D graphics environment, *Comput. Sci. Eng.*, 9, 90-95,  
362 <https://doi.org/10.1109/MCSE.2007.55>, 2007.
- 363 Liu, Y., Zhou, M., Zhao, S., Zhan, W., Yang, K., and Li, M.: Automated extraction of tidal  
364 creeks from airborne laser altimetry data, *J. Hydrol.*, 527, 1006-1020,  
365 <https://doi.org/10.1016/j.jhydrol.2015.05.058>, 2015.
- 366 Marani, M., D’Alpaos, A., Lanzoni, S., Carniello, L., and Rinaldo, A.: Biologically-controlled  
367 multiple equilibria of tidal landforms and the fate of the Venice lagoon, *Geophys. Res.*  
368 *Lett.* 34, L11402, <https://doi.org/10.1029/2007gl030178>, 2007.
- 369 Maximova, T., Vanlede, J., Plancke, Y., Verwaest, T., and Mostaert, F.: Inrichtingsplan  
370 Hedwige-Prosperpolder: Deelrapport 1 – Numeriek 2D model, *WL Rapporten*, 13\_166,  
371 Flanders Hydraulics Research, Antwerp, Belgium, 2014.
- 372 Richardson, A.D., Braswell, B.H., Hollinger, D.Y., Jenkins, J.P., and Ollinger, S.V.: Near-surface  
373 remote sensing of spatial and temporal variation in canopy phenology, *Ecol. Appl.*, 19,  
374 1417-1428. <https://doi.org/10.1890/08-2022.1>, 2009.
- 375 Rinaldo, A., Fagherazzi, S., Lanzoni, S., Marani, M., and Dietrich, W.E.: Tidal networks: 2.  
376 Watershed delineation and comparative network morphology, *Water Resour. Res.*, 35,  
377 3905-3917, <https://doi.org/10.1029/1999wr900237>, 1999.
- 378 Silinski, A., van Belzen, J., Fransen, E., Bouma, T.J., Troch, P., Meire, P., Temmerman, S.:  
379 Quantifying critical conditions for seaward expansion of tidal marshes: A transplantation

380 experiment. *Estuar. Coast. Shelf S.*, 169, 227-237,  
381 <https://doi.org/10.1016/j.ecss.2015.12.012>, 2016.

382 Van de Broek, M., Vandendriessche, C., Poppelmonde, D., Merckx, R., Temmerman, S., and  
383 Govers, G.: Long-term organic carbon sequestration in tidal marsh sediments is  
384 dominated by old-aged allochthonous inputs in a macrotidal estuary, *Global Change*  
385 *Biol.*, 24, 2498-2512. <https://doi.org/10.1111/gcb.14089>, 2018.

386 Vandenbruwaene, W., Vanlede, J., Plancke, Y., Verwaest, T., and Mostaert, F.:  
387 Inrichtingsplan Hedwige-Prosperpolder: Deelrapport 3 – Empirisch ophogingsmodel, WL  
388 Rapporten, 13\_166, Flanders Hydraulics Research, Antwerp, Belgium, 2014.

389 van Leussen, W.: The variability of settling velocities of suspended fine-grained sediment in  
390 the Ems estuary. *J. Sea Res.* 41, 109-118. [https://doi.org/10.1016/s1385-1101\(98\)00046-](https://doi.org/10.1016/s1385-1101(98)00046-x)  
391 [x](https://doi.org/10.1016/s1385-1101(98)00046-x), 1999.

392 Zhou, Z., van der Wegen, M., Jagers, B., and Coco, G.: Modelling the role of self-weight  
393 consolidation on the morphodynamics of accretional mudflats, *Environ. Modell. Softw.*,  
394 76, 167-181. <https://doi.org/10.1016/j.envsoft.2015.11.002>, 2016.